

Seasonal Variability of Snow Cover and Impact on Albedo and Thermal Properties in the Antarctic Marginal Ice Zone

Ippolita Tersigni¹, Filippo Nelli², Emiliano Cimoli³,
 Petra Heil⁴, Luke Bennetts⁵, Giulio Passerotti⁶,
 Alessandro Toffoli¹

¹Department of Infrastructure Engineering, The University of Melbourne, Parkville, VIC 3010, Australia

²Department of Mechanical and Product Design Engineering, School of Engineering, Swinburne University of Technology, Hawthorn, VIC 3122, Australia

³Institute for Marine and Antarctic Studies, College of Sciences and Engineering, University of Tasmania, Hobart, TAS 7001, Australia

⁴Australian Antarctic Division, Department of Climate Change, Energy, the Environment and Water, Kingston, TAS, Australia

⁵School of Mathematical Sciences, University of Adelaide, Adelaide, SA, Australia

⁶School of Computing and Information Systems, The University of Melbourne, Parkville, VIC 3010, Australia

Abstract

Snow cover plays a critical yet often underrepresented role in shaping the thermodynamic behavior of Antarctic sea ice. In this study, we investigate the seasonal variability of snow distribution and its impact on surface albedo and energy fluxes across the marginal ice zone (MIZ), using a unique dataset from five shipborne expeditions conducted between 2019 and 2024. High-resolution visible and infrared imagery, combined with field observations and meteorological data, reveal that even modest snow fractions substantially increase surface reflectivity and suppress conductive heat transfer. Our results demonstrate that simplified binary assumptions—such as assigning dry snow in winter and bare ice in summer—systematically misrepresent surface conditions, introducing significant biases in modelled radiative and turbulent fluxes. By explicitly resolving fractional snow cover, we show that surface albedo and energy exchange respond nonlinearly to snow–ice composition, with implications for sea ice growth, melt, and climate feedbacks. These findings advocate for a revision of current model parameterizations, emphasizing the need for multi-component surface schemes that reflect the observed heterogeneity of the Antarctic MIZ.

1 Introduction

Sea ice is a key component of the Earth’s climate system, mediating exchanges of energy, momentum, and gases between the ocean and atmosphere. Its high albedo reflects a large portion of incoming solar radiation, significantly influencing the surface energy budget Curry et al. [1995], Stroeve et al. [2012], Notz and Stroeve [2016]. Antarctic sea ice differs significantly from its Arctic counterpart: it is thinner, more dynamic, and predominantly seasonal, with greater exposure to wind and wave forcing Worby et al. [2008]. Formed in the open Southern Ocean, it is also characterized by a more extensive and variable snow cover due to higher atmospheric moisture and frequent precipitation events Massom and Stammerjohn [2001], Sturm et al. [1995], Warren et al. [1999]. The snow layer acts as a key modulator of the energy balance of the sea ice surface, altering both the albedo and thermal conductivity, thus influencing the rate of growth and melting of the underlying ice Sturm et al. [1995]. The surface albedo, in particular, is highly sensitive

to the presence and physical properties of snow and depends considerably on the season, the grain size of the snow, the melt processes, and the type of surface, such as dry snow and bare ice Ebert and Curry [1993], Light et al. [2008], Nicolaus et al. [2010]. The low thermal conductivity of snow acts as an effective insulator that significantly modulates the vertical heat flux through the ice. During winter, the presence of a strong temperature gradient between the relatively warm ocean and the much colder atmosphere drives the *upward* conductive heat flux from the ocean to the atmosphere through the ice. The snow layer reduces the heat loss by impeding conduction, thereby slowing the rate of ice growth despite the steep thermal gradient Sturm et al. [1995], Maykut and Untersteiner [1971]. In summer, when the temperature gradient is reversed and directed *downward* from the warmer atmosphere toward the ice surface, the snow layer limits heat absorption primarily by reflecting the majority of incoming solar radiation due to its high albedo. However, a small fraction of solar energy is still absorbed, and along with additional inputs from atmospheric longwave radiation and sensible heat, this energy gradually warms the snow. Once the snow reaches the melting point, further energy is used to overcome the latent heat of fusion, causing the warming and melting of the underlying sea ice Wiscombe and Warren [1980], Brandt and Warren [1993], Sturm et al. [2002]. These insulating and radiative effects make snow cover a central driver of the seasonal thermodynamic evolution of sea ice. The effects of albedo and thermal conductivity become particularly crucial in the Antarctic Marginal Ice Zone (MIZ), where the heterogeneity of surface conditions strongly influences physical processes. This heterogeneity, driven by wave–ice interactions, variable ice concentrations, and intermittent snow cover, modulates both the surface reflectivity and the surface interactions between the ocean, ice, and atmosphere Tersigni et al. [2023], Squire [2007], Williams et al. [2013], Horvat and Tziperman [2016]. Recent high-resolution thermal imaging has revealed the fine-scale variability of surface temperatures in the MIZ and demonstrated how this spatial heterogeneity drives turbulent heat fluxes at the air–ice interface Tersigni et al. [2023].

Despite its climatic importance, the MIZ remains challenging to represent in climate models Horvat and Tziperman [2016], Williams et al. [2013], largely due to the high degree of spatial and temporal heterogeneity in surface conditions, which complicates the parameterization of albedo and snow–ice interactions. The representation of sea ice surface conditions in global forecasting and climate models necessarily relies on simplifying assumptions, which are essential for ensuring computational feasibility and model stability ECMWF [2021], Dutra et al. [2010]. However, these assumptions often overlook the fine-scale heterogeneity observed in the field, particularly concerning snow cover, surface type, and the associated thermodynamic processes Light et al. [2008], Tersigni et al. [2023]. For instance, the Integrated Forecasting System (IFS) used by the European Centre for Medium-Range Weather Forecasts (ECMWF) prescribes monthly sea ice surface albedo values based on the parameterization developed by Ebert and Curry [1993]. Dry-snow albedo values are used for the winter months, while bare ice albedo values are prescribed to represent summer conditions. The integrated albedo of dry snow is modeled as a function of the solar zenith angle, with a maximum value of 0.82 under full ice cover and direct solar radiation Ebert and Curry [1993]. For diffuse radiation, dry-snow albedo values are taken from Shine and Henderson-Sellers [1985]. In contrast, bare ice albedo is defined using a theoretical logarithmic function of sea ice thickness. However, this binary seasonal classification does not account for the spatial and temporal variability observed in sea-ice environments. Resulting biases include overestimation of absorbed shortwave radiation and underestimation of sea ice albedo Batrak and Müller [2018], Eustace et al. [2024], undermining the reliability of surface energy budget simulations.

This study investigates the seasonal variability of snow cover in the Antarctic marginal ice zone (MIZ) and its impact on surface albedo and thermal properties. We analyze a unique dataset collected during five shipborne expeditions along the Atlantic and the East Antarctic sectors of the Southern Ocean in Winter 2019, Winter 2022, Spring 2019, Spring 2024, and Summer 2024. Field data were acquired using an integrated camera system including optical,

multispectral, and thermal infrared sensors. We characterize the spatial distribution of dry snow and bare ice on sea ice and evaluate their combined influence on surface albedo and heat fluxes. By treating the snow–ice surface as a composite system, our analysis captures seasonal variability and coexisting surface types, offering new insight into their radiative and thermal behavior in the MIZ.

2 Method

2.1 Measurement campaigns

This study is based on shipborne observations collected during five Antarctic expeditions between 2019 and 2024, spanning cold and warm seasons. Three field campaigns were conducted in collaboration with the University of Cape Town under the Southern Ocean seasonal Experiment (SCALE) project as part of the South African National Antarctic Programme (SANAP) Ryan-Keogh and Vichi [2022] aboard the *S.A. Agulhas II* icebreaker. The expeditions took place in the Eastern Weddell Sea, departing from Cape Town, South Africa (33.9°S , 18.5°E). In July 2019, during peak winter, the *S.A. Agulhas II* encountered the ice edge at 56.5°S , progressing into consolidated ice with widespread fresh snow cover (Figure 1a). A second voyage in October–November 2019, during the late melt season, traversed a dynamic MIZ, observing intermittent ice floes and compact snow-covered ice near 55.8°S (Figure 1b). The third campaign in July 2022 followed a similar route to winter 2019, reaching the ice edge near 57°S and recording conglomerated pancakes with wet snow cover, highlighting the interannual variability (Figure 1c). The last two missions were part of the Ocean–Sea Ice–Atmosphere (OSIA) project supported by the Australian Antarctic Program (AAP) onboard the *RSV Nuyina* research vessel. The expeditions were carried out on the Davis and Mawson seas, which straddle the Indian and the Western Pacific Ocean. The summer campaign (February–March 2024) departed from Hobart, Australia (42.9°S , 147.3°E), entering the seasonal ice zone en route to Casey, Davis, and Mawson research stations. Observations were concentrated near the eastern ice edge (64°S), where sparse sea ice included small pancakes and fresh snow on newly formed ice (Figure 1d). A final expedition in October–November 2024 followed the same transect of the previous voyage but did not reach Mawson Station. It captured the seasonal transition from melt to refreeze, with more extensive sea ice concentrations dominated by first-year ice and large pancakes. The MIZ was located further north, near 58°S (Figure 1e).

During each expedition, a shipborne camera system was used to monitor the sea ice surface. The primary system included a monochrome industrial CMOS camera operating in the visible range (see Alberello et al. [2019, 2022]) and a Telops FAST-IR thermal imaging camera for infrared measurements (see Tersigni et al. [2023]). The visible camera provided a $\sim 90^{\circ}$ field of view and was mounted on the monkey bridge of the *S.A. Agulhas II* at an elevation of $\sim 25\text{m}$ above the waterline with an inclination of 30° . On the *RSV Nuyina* the same camera was mounted port-side on the bridge at $\sim 37\text{m}$, inclined at 25° relative to the horizon. Images were acquired at 2448×2048 pixel resolution and 2 Hz sampling, continuously recorded with Coordinated Universal Time (UTC) timestamps. The thermal infrared camera was mounted port-side at $\sim 16\text{m}$ above the waterline with an inclination of $\sim 40^{\circ}$ on the *S.A. Agulhas II* and at $\sim 34\text{m}$ and inclined at 18° on the *RSV Nuyina*. The IR camera recorded skin temperature data at a resolution of 640×512 pixels and 2 Hz for 20-minute intervals every three hours. Its spectral range covered $7.5\text{--}13.5\mu\text{m}$. During the two spring and summer 2024 voyages aboard the *RSV Nuyina*, two additional sensors were installed and used in this study only for data validation. A TOUCAN multispectral camera, covering 400–900 nm, was installed port-side on deck nine at $\sim 34\text{ m}$ (inclination: 23°) to analyze surface reflectance. A second monochrome visible camera with optical zoom, also installed on deck nine (inclination: 46°), was used to estimate ice thickness during icebreaking operations.

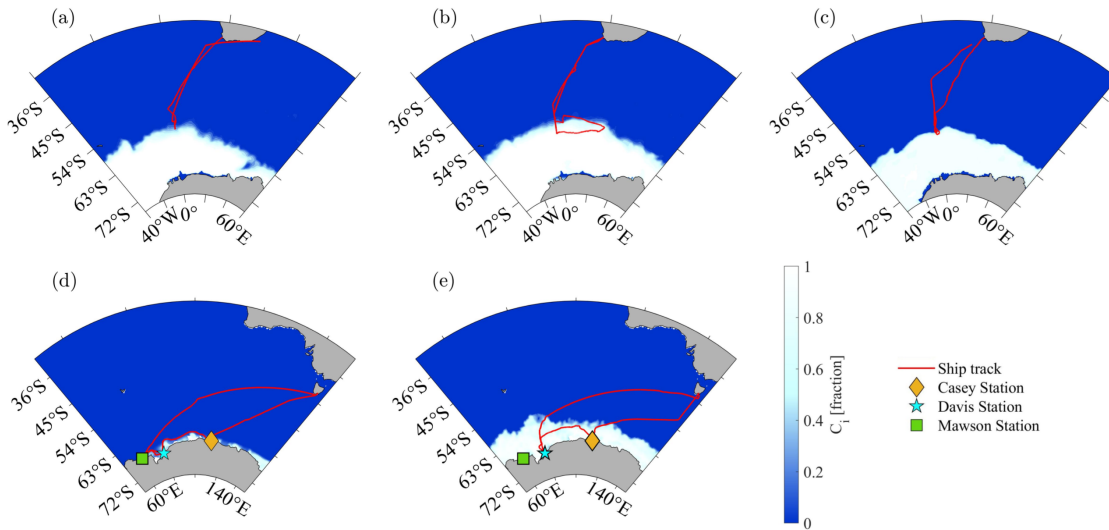


Figure 1: Ship tracks (red lines) of fieldwork expeditions over the sea ice concentration maps for different Antarctic research expeditions. Panels (a–c) show ship tracks in the Atlantic sector of the Southern Ocean onboard the S.A. Agulhas II icebreaker in July 2019 (a), October–November 2019 (b), and July 2022 (c). Panels (d–e) show ship tracks in the East Antarctic sector onboard the RSV Nuyina icebreaker in February–March 2024 (d) and October–November 2024 (e). The background shading represents sea ice concentration (C_i) [0–1], with darker blue indicating open ocean and lighter shades indicating higher sea ice coverage. The locations of Antarctic research stations are marked: Casey Station 66.3°S , 110.5°E (yellow diamond), Davis Station 68.6°S , 78.0°E (blue star), and Mawson Station 67.6°S , 62.9°E (green square).

Hourly visual observations of sea ice conditions were conducted during all five expeditions following the standard ASPeCt protocol (Antarctic Sea Ice Processes and Climate; Worby and Comiso [2004]). Observers recorded sea ice properties within a \sim 1-km radius of the vessel, including total ice concentration, up to three distinct ice types, floe size distribution, surface topography, snow type, ice thickness, and snow thickness when present. Snow and ice thickness estimates were made when floes were overturned or broken by the ship’s passage, using reference objects such as the ship’s 1 m waterline stick and a suspended reference ball, as introduced by Allison [1989]. In this study, particular emphasis was placed on the measurement of snow cover, visually estimated as the fractional area of snow-covered ice within the observation zone. Despite their subjective nature, these estimates were critical for interpreting automated camera data and served as an independent validation of surface type classifications, especially under the heterogeneous conditions typical of the marginal ice zone. Each observation was georeferenced using GPS coordinates, with timestamps recorded in Coordinated Universal Time (UTC), enabling precise temporal alignment with shipborne camera data and satellite imagery for cross-platform comparison.

2.2 Data analysis

2.2.1 Quality Control and Initial Filtering

The initial phase of data processing involved rigorous quality control procedures applied to the raw imagery collected by each camera. For visible images (stored in JPEG format), a filtering procedure was implemented to exclude low-quality frames. Images acquired during nighttime or degraded by poor visibility, lens contamination (e.g., water droplets, sea spray, salt, snow, or dirt), motion blur, or atmospheric disturbances (e.g., fog or precipitation), were systematically

discarded. The 72% of the total stereo image dataset passed this quality control step and were retained for subsequent analysis. The IR images were collected in proprietary format files (.hcc), which were first screened for integrity before decoding. Files containing corrupted metadata, lens contamination, or atmospheric disturbances were removed. After quality control, the 64% of the IR files were retained.

2.2.2 Orthorectification, Segmentation, and Pixel Classification

The visible sea ice images that passed the initial quality check were orthorectified to correct for perspective distortion and non-uniform scaling introduced by the viewing geometry of the camera following the approach described in Passerotti et al. [2024]. This step was essential to eliminate the artificial distortion of ice floes in the foreground and the compression of those farther from the camera, ensuring that each pixel accurately represented a consistent ground area. Orthorectified images were then segmented using the Segment Anything Model (SAM), a deep learning-based vision foundation model developed by Meta AI for general-purpose segmentation. SAM algorithm automatically identified and outlined distinct features in each image by recognizing patterns it had learned from a large training dataset, without requiring predefined contours or manual input. Implemented in Python, SAM automatically produced binary masks isolating surface features such as floes, leads, and snow-covered regions. These segmentation masks were then subjected to pixel-based classification based on greyscale intensity. Reflectance differences were leveraged to distinguish between snow and non-snow surfaces: snow was identified as the optically brightest class, while bare ice and other features exhibited lower brightness levels. A fixed intensity threshold, determined empirically, was used to compute the fractional snow cover for each image as the proportion of pixels classified as “snow” Passerotti et al. [2024]. In some cases, the segmentation algorithm failed to produce reliable masks due to low contrast, complex illumination, or ambiguous surface patterns. As a result, approximately 25% of the orthorectified visible images were discarded at this stage to ensure the accuracy of the derived snow cover estimates. Orthorectification was not applied to the thermal images, as temperature measurements are not affected by perspective distortion in the same manner as spatial features in visible imagery. Furthermore, segmentation was not necessary, as the objective was to characterize the temperature of the entire sea ice surface, including snow-covered areas, bare ice, melt ponds, and leads, rather than isolating specific surface types. IR data were processed in MATLAB by decoding each .hcc file into a 2D IR image. Each pixel represents the surface skin temperature at a spatial resolution of approximately 10 cm, corresponding to the top 10 mm of the surface. To ensure the integrity of the thermal signal, peripheral regions of the images were systematically excluded from analysis. Specifically, the lower portion of each thermal frame was cropped to eliminate radiative contamination from the ship’s warm hull and wake, while the upper portion was excluded to avoid the influence of the horizon and distant surfaces that were poorly resolved or partially obscured. The resulting central region of each image was retained in its native pixel geometry and used for quantitative analysis of surface temperature variability across the field of view.

2.2.3 Aggregation and Temporal Matching

To integrate data from the multiple imaging systems into a consistent dataset suitable for analysis, a temporal alignment procedure was applied across all retained observations. Since the cameras operated independently, only images acquired within a tightly defined temporal window of ± 1 hour were considered valid for combined analysis. This ensured that each composite data point represented a consistent scene under the same ocean and atmospheric conditions. Matched images, cases where all sensors captured usable data within the time same ± 1 hour window, were retained for downstream processing. This strict temporal co-registration criterion reduced the final usable dataset to approximately 15% of the total image archive. For each of

these matched records, the outputs from the camera system (classified snow fraction and skin temperature) were integrated to generate a unified set of surface parameters. All composite records were then georeferenced by associating each data point with the ship's GPS-derived location (latitude and longitude) recorded at the corresponding UTC time. Positional data were obtained from the South African Weather Service (SAWS), which operates a dedicated observation system onboard the S.A. Agulhas II icebreaker Ryan-Keogh and Vichi [2022]. For expeditions conducted onboard the RSV Nuyina vessel, ship position data were recorded by the Underway Voyage Data archive provided by the Australian Antarctic Division (AAD), which compiles continuous environmental and navigational measurements. This ensured that each entry in the final dataset was both temporally and spatially resolved, enabling consistent mapping and environmental correlation in subsequent analyses.

2.2.4 Derivation of Physical Quantities

The final stage of data analysis involved the computation of key geophysical parameters from the integrated dataset. Surface properties derived from image-based classification, including fractional snow cover and skin temperature, were combined with atmospheric and oceanographic variables measured by the ships' onboard instruments to derive physically relevant quantities such as integrated surface albedo and surface energy fluxes. The research vessels were equipped with comprehensive suites of meteorological and oceanographic instruments to support continuous environmental monitoring throughout the expeditions. Atmospheric measurements used in this study included air temperature, relative humidity, wind speed, and barometric pressure. These variables were recorded using ultrasonic anemometers, barometers, air temperature and humidity probes, and pyranometers and pyrgeometers for incoming and outgoing shortwave and longwave radiation. Oceanographic data, including sea salinity and conductivity, were collected using thermosalinographs and Conductivity-Temperature-Depth (CTD) profilers integrated into the ships' underway systems. Ice and snow thickness were estimated from visual observations conducted under the ASPeCt protocol.

The integrated surface albedo α was estimated following the parameterization described in Ebert and Curry [1993], where the albedo is computed as the weighted sum of spectral albedos over distinct shortwave wavelength bands. Specifically, albedo was calculated as:

$$\alpha = \sum_{j=1}^4 \alpha_j w_j \quad (1)$$

where α_j is the spectral albedo for each band j and w_j is the corresponding weight representing the fractional contribution of solar irradiance in that band. The spectral bands and weighting factors were taken directly from *Table 2. Spectral Albedos for Five Surface Types* in Ebert and Curry [1993], which defines four shortwave bands spanning 0.25 to 4.00 μm . Each band is associated with spectral albedo parameterizations for different surface types, including *Dry snow*, separating direct (solar zenith-angle dependent) and diffuse (fixed) radiation, and *Bare sea ice*, modeled as a function of ice thickness for $h < 2\text{m}$. Surface albedo was calculated using the physical variables extracted from the corresponding 20-minute sequence of field observations. The dry snow albedo parameterization was applied to the average fraction of snow-covered surface, and the bare ice parameterization to the average fraction of bare ice, using the spectral albedo equations 1. The resulting broadband albedo was computed as the area-weighted sum of the contributions from the two surface types. The field-observed surface albedo was calculated by weighting the integrated albedos of dry snow and bare ice according to their respective fractional surface coverage effectively observed in each sequence, thereby accounting for the spatial heterogeneity of the sea ice surface.

The components of the surface energy fluxes were calculated following the parameterizations described in Worby and Allison [1991], which provides bulk formulations suitable for estimating

the air-ice-ocean interactions over thin Antarctic sea ice. The computed fluxes, measured in Joules per second per square meter [Wm^{-2}], include net short wave radiation (F_{sw}), conductive heat flux (F_c), net longwave radiation (F_{lw}), latent heat flux (F_e), and sensible heat flux (F_s).

F_{sw} represents the portion of incoming solar radiation that is absorbed by the surface after accounting for the albedo (α) and the fraction of energy transmitted into the sea ice (I_o). It is calculated as follows:

$$F_{sw} = (1 - \alpha)(1 - I_o)F_r \quad (2)$$

To estimate I_o , we adopted an empirical parameterization based on cloud cover fraction (C) and solar zenith angle (Θ_n), following the approach in Maykut and Untersteiner [1971], Ebert and Curry [1993] where:

$$I_o = 0.62 \cdot C + 0.0019 \cdot \Theta_n \quad (3)$$

The variable C was measured by the onboard weather station in oktas (ranging from 0 to 8), and then converted to a fractional scale (0 to 1) for use in the transmissivity calculation.

The solar zenith angle Θ_n was calculated from the ship's geographic coordinates and observation UTC times using standard solar position algorithms based on astronomical geometry. This angle represents the deviation of the Sun from the vertical. To compute Θ_n , we used the following relation from Iqbal [2012]:

$$\cos(\Theta_n) = \sin(\phi) \sin(\delta) + \cos(\phi) \cos(\delta) \cos(h) \quad (4)$$

where ϕ is the latitude of the observation point (degrees), δ is the solar declination angle (degrees), and h is the hour angle (degrees), derived from local solar time. Solar declination and hour angle were computed at each timestamp using solar ephemeris formulas.

The incoming shortwave radiation at the surface (F_r) was estimated from ship-based measurements of photosynthetically active radiation (PAR). PAR sensors mounted on the vessel measured downwelling visible light in the 400- 700 nm range, which represents only part of the total solar spectrum. To convert these measurements into total shortwave radiation, we followed the approach described by Kirk [1994], where PAR is assumed to represent approximately 45-50% of the total solar irradiance, depending on atmospheric conditions and solar zenith angle. The measured PAR flux (in $\mu\text{mol photons m}^{-2} \text{s}^{-1}$) was first converted to energy units (joules) using the factor $4.57 \mu\text{mol J}^{-1}$. This step gives the visible light energy. To estimate total solar radiation, we then applied a spectral correction factor 2.1, to account for the additional energy in the ultraviolet and infrared parts of the spectrum. The resulting values of F_r represent the incoming solar energy in W m^{-2} , referenced to the horizontal surface.

F_c represents the vertical transfer of heat through the snow and ice, driven by temperature gradients. In this study, F_c was calculated considering the sea ice surface as a layered system of snow over ice, with total flux derived from the combined conductive contributions of both layers. We used F_c as follows:

$$F_c = \frac{k_s}{H_s} + \frac{\left(k_o + \frac{\beta S_o}{T_o - 273}\right)}{H_i} (T_b - T_o) \quad (5)$$

where k_s is the thermal conductivity of snow, here we adopted a representative constant value of $0.31 \text{ W m}^{-1} \text{ K}^{-1}$, consistent with Calonne et al. [2019], Sturm et al. [1997], H_s is the snow thickness (m), k_o is the thermal conductivity of pure ice which quantifies the rate of conductive heat transfer through the sea ice column. We used a fixed value of $2.03 \text{ W m}^{-1} \text{ K}^{-1}$ following the parameterization adopted in Maykut and Untersteiner [1971], $\beta = 0.117 \text{ W m}^{-2} \text{ kg}^{-1}$ is a constant. S_o is the bulk salinity of sea ice (g/kg), T_o is the surface temperature of the ice (K), T_b is the freezing point (-1.8°C), and H_i is the ice thickness (m).

F_{lw} was calculated as the difference between incoming and outgoing longwave radiation:

$$F_{lw} = e_a \sigma T_a^4 - \epsilon \sigma T_{sk}^4 \quad (6)$$

where ϵ_a is the atmospheric emissivity, estimated as $\epsilon_a = 0.934 + 0.036\sqrt{e}$, with e being the vapor pressure derived from relative humidity and air temperature using the Tetens equation Murray [1967], Crawford and Duchon [1999]. The term ϵ is the longwave emissivity of the surface, for which we used values of 0.99 for dry snow and 0.97 for bare ice. T_a is the air temperature, and T_{sk} is the surface skin temperature, both expressed in Kelvin. Unlike Worby and Allison [1991], who included an empirical scaling factor of 1.38 in the longwave radiation term to correct for underestimation in polar conditions, we did not apply this coefficient. This choice was made to preserve consistency with the Stefan–Boltzmann law, given that our formulation already accounts for atmospheric water vapor through the parameterization of ϵ_a .

F_e was calculated using the bulk aerodynamic formulation:

$$F_e = \rho L_v C_e U (q_s - q_a) \quad (7)$$

where ρ is the air density (kg m^{-3}), L_v is the latent heat of sublimation ($2.835 \times 10^6 \text{ J kg}^{-1}$), and U is the wind speed at 10 m height (m s^{-1}). The transfer coefficient C_e was set to 0.0011 over snow surfaces and 0.0014 over bare ice, to reflect differences in surface roughness and turbulent exchange Brunke et al. [2006]. q_s is the surface specific humidity, assumed to be at saturation for the given skin temperature, and q_a is the specific humidity of the near-surface air, calculated from air temperature, pressure, and relative humidity Murray [1967]. This formulation follows the standard bulk aerodynamic approach for turbulent fluxes Talley [2011].

F_s was calculated using the bulk aerodynamic formulation:

$$F_s = \rho c_p C_h U (T_{sk} - T_a) \quad (8)$$

where ρ is the air density (kg m^{-3}), c_p is the specific heat capacity of air at constant pressure ($1005 \text{ J kg}^{-1} \text{ K}^{-1}$), U is the wind speed at 10 m height (m s^{-1}), T_{sk} is the skin temperature, and T_a is the near-surface air temperature (both in Kelvin). The transfer coefficient C_h was set to 0.0013 over snow surfaces and 0.0015 over bare ice, to reflect differences in aerodynamic roughness and turbulent heat exchange Brunke et al. [2011].

Finally, F_T represents the net energy exchange between the atmosphere and the surface and was calculated as the sum of all radiative and turbulent flux components. A positive F_T indicates a net gain of energy by the surface, while a negative Q_T indicates a net loss.

2.3 Data validation

As introduced in the 2.1 section, a multispectral camera and a monochromatic camera with optical zoom are used to validate snow distribution and ice thickness measurements. To validate the snow cover fraction estimated using the SAM classification algorithm (described in 2.2.2), we compared it against an independent method based on multispectral imagery acquired by the TOUCAN camera system, installed on board the *RSV Nuyina* during the February–March 2024 voyage. This camera recorded continuous imagery across ten spectral bands (400–900nm) in the visible and near-infrared (VNIR) range. After quality control, retaining approximately 35% of the dataset, images were processed using a seeded KMeans clustering algorithm ($k = 4$), trained iteratively on representative scenes to account for varying illumination Cimoli et al. [2017, 2019, 2020]. The algorithm classified each frame into four optically distinct surface categories: *pure snow*, *wet snow*, *bare ice*, and *open water*. Classification outputs were verified visually using RGB composites (bands 2, 4, and 7) for consistency as shown in Figure 2a, while an example of the SAM-based segmentation applied on the same frame is shown in Figure 2b. Thirty sequences of 20-minute multispectral images and processed each sequence using both the KMeans methods

and SAM for data validation. The resulting snow cover fractions were compared via scatterplot Figure 2(c), obtaining a root mean square error (RMSE) of 0.107 and a mean bias error (MBE) of 0.012. This agreement confirms the robustness of the SAM-based classification for estimating snow cover fraction across different surface and illumination conditions.

To evaluate the accuracy of the ice thickness estimates derived from ASPeCt visual observations, we used a secondary dataset acquired by the monochrome camera with optical zoom, installed on board the *RSV Nuyina*. This camera captured sequences of floes overturned during icebreaking operations, exposing clear vertical ice profiles. A custom image analysis pipeline was applied to extract ice thickness automatically. The pipeline incorporated geometric camera calibration and orthorectification based on known intrinsic and extrinsic parameters (e.g., focal length, tilt, elevation), enabling consistent pixel-to-distance conversion ($1\text{px} = 1\text{cm}$) across all images. Overturning ice events were automatically segmented using a fine-tuned version of SAM, where only the mask decoder was retrained using 256 manually annotated image–mask pairs. This specialized model enabled robust identification of overturning ice slabs with minimal false positives. Post-processing filters were applied to eliminate noisy or ambiguous masks, retaining only clean and isolated floe profiles. For each segmented object, ice thickness was estimated by drawing multiple transects across the short edge of the bounding box and averaging the resulting measurements to minimize edge irregularities and segmentation noise, as shown in Figure 2d–e. Following quality filtering, only approximately 5% of the original dataset yielded valid ice thickness estimates. Due to this limited yield, ASPeCt visual observations were used to complement the dataset and ensure adequate coverage. We identified overlapping observations between the zoom camera and ASPeCt protocol measurements. A comparison of ice thickness values (Figure 2f) showed strong agreement, with a mean bias error (MBE) of 0.006m and a root mean square error (RMSE) of 0.088m. These results confirm the accuracy of the ASPeCt-derived visual estimates and validate their use as a reliable reference for ice thickness in this study.

3 Results

3.1 Snow distribution on sea ice MIZ

Our observations indicate that snow cover on Antarctic sea ice is characterized by pronounced spatial and temporal variability. This heterogeneity is caused by the interaction between highly dynamic weather conditions such as episodic snowfall, strong winds, and transient warming events, and the physical structure of the sea ice surface. Even during winter, air temperatures can approach or exceed 0°C Tersigni et al. [2023], allowing for partial melt and refreeze processes that further influence snow redistribution. Wind-driven transport plays a central role in eroding and relocating freshly fallen snow, often concentrating it on thicker or more stable ice while leaving thinner floes, leads, and nilas largely exposed Massom and Stammerjohn [2001]. These processes result in a patchy and discontinuous snow cover, particularly evident in the marginal ice zone (MIZ), which is not governed by seasonality and where ice types and surface roughness vary over short distances. Figure 3 shows the probability density functions (pdfs) of fractional snow cover derived from visible imagery for each expedition, highlighting seasonal and interannual variability across the Antarctic marginal ice zone (MIZ). Panels (a–e) correspond to July 2019, July 2022, October–November 2019, October–November 2024, and February–March 2024, respectively. Representative grayscale images above each panel illustrate typical surface conditions associated with specific snow cover fractions measured during acquisition. During the winter 2019 campaign (Figure 3a), the snow cover distribution exhibits a trimodal structure, reflecting distinct surface regimes along the meridional transect. At 56.5°S , scenes with 0% snow cover correspond to small (less than 1m), thin pancakes ice. A second peak near 65% is associated with larger pancakes (2–3 m diameter) partially covered by snow; these floes were typically observed near 57°S and showed signs of overwash along their edges. The third peak, around

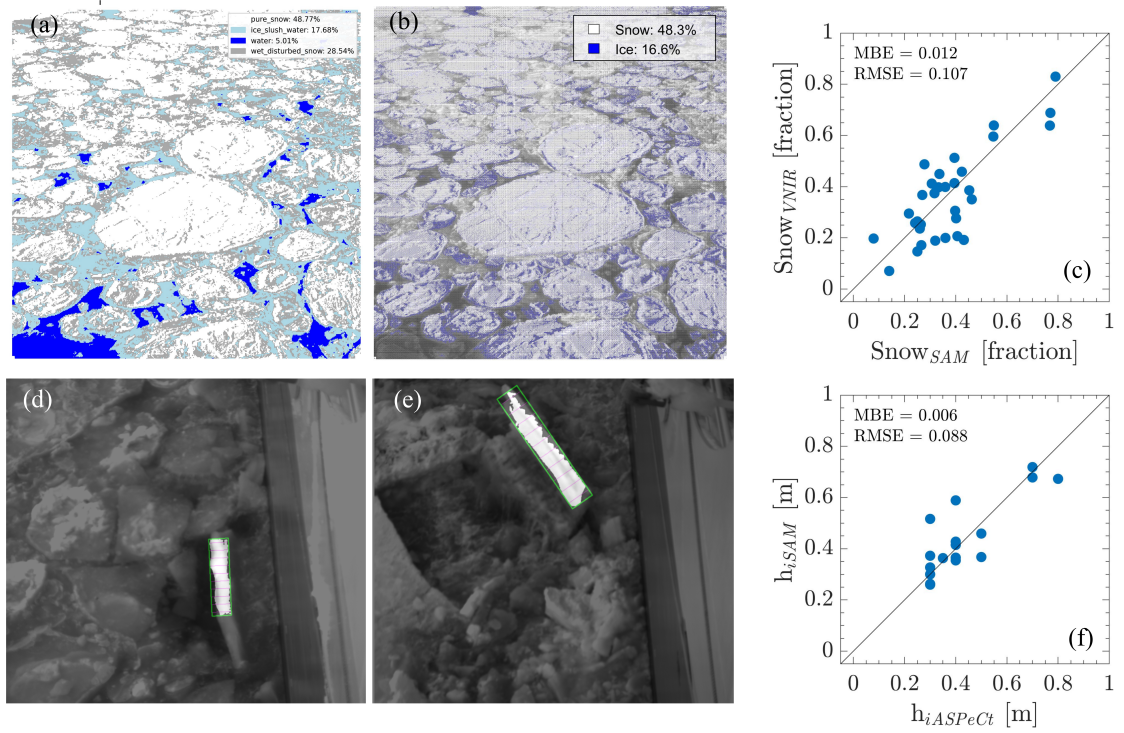


Figure 2: Validation of snow cover fraction and ice thickness estimated from the SAM classification algorithm. (a) Multispectral VNIR classification of surface types, with categories: pure snow (white), wet/disturbed snow (light gray), ice/slush/water (light blue), and water (dark blue). (b) Classified surface types from SAM applied to visible imagery, showing snow (white) and ice (blue) fractions. (c) Scatterplot comparing snow fraction derived from VNIR and SAM methods ($MBE = 0.012$; $RMSE = 0.107$). (d–e) Example ice thickness measurements obtained from overturning ice events detected and segmented by SAM, showing transects used for thickness estimation. (f) Scatterplot comparing ice thickness derived from SAM and ASPeCt observations ($MBE = 0.006$; $RMSE = 0.088$)

100%, corresponds to compact ice with full snow cover observed farther south (58°S). In winter 2022 (Figure 3b), the distribution broadens and flattens, with more frequent low and intermediate snow cover. Ninas ice with 0–10% snow cover dominated the transect near 59°S . Moderate snow fractions (40–60%) were observed over pancake ice at 59.3°S , while extensive snow coverage (80–100%) appeared on conglomerated floes near 59°S . The spring 2019 distribution (Figure 3c) shifts markedly toward higher snow fractions, with a dominant mode near 95% associated with compact ice at 58.5°S . Nevertheless, snow heterogeneity persists, particularly in the form of nillas with 0–20% cover observed at 58.4°S and large pancakes (up to 5 m diameter) with 40–60% cover at 58°S . By spring 2024 (Figure 3d), the distribution becomes strongly skewed toward low snow fractions, peaking at 0–10%, predominantly between 64 – 68°S . Most of the observed surface consisted of melting nillas and newly formed ice with little or no snow. Snow-covered regions were limited to isolated patches of first-year ice near 66°S approaching Davis Station. The summer 2024 distribution (Figure 3e) maintains a similar skew, with a strong peak near 5% and minimal incidence of high snow fractions. Observations were dominated by small pancake ice in new formations near 67°S , with negligible snow presence. Snow was only observed on young grey ice and first-year ice at 67 – 68°S . The relationship between snow cover versus sea ice concentration and floe size is shown in the boxplot in Figure 4a-b. Combining the data from all the missions, we observe no significant dependence of snow cover on ice concentration and floe size: the median and interquartile ranges remain consistent across the 50–90% concentration range. This suggests that snow presence is not strictly correlated with total ice coverage and instead reflects more localized surface processes and ice floe characteristics.

3.2 Impact of snow on albedo

Figure 5 compares observed surface albedo values with model-based assumptions (see Table 2, in Ebert and Curry [1993]), highlighting the role of snow cover, ice thickness, and surface type in modulating reflectivity across seasons in the Antarctic MIZ. Panels (a) and (b) assess the deviation between observed albedo and simplified model assumptions. Specifically, the x-axis in both panels shows $\alpha_{\text{SnowandIce}}$, the observed albedo computed as the area-weighted average of dry snow and bare ice components based on their fractional surface coverage. In panel (a), albedo values observed during the winter seasons are compared against α_{DrySnow} value, which assumes a uniform snow-covered surface, typically used by models in winter parameterizations. The 1:1 line indicates perfect agreement. Most data points fall above this line, revealing that α_{DrySnow} consistently overestimates the albedo, especially in free-snow or partially snow-covered scenes (dark blue dots). The comparison improved for pancakes and young ice covered by snow for more than 80% (light blue dots). Panel (b) compares the $\alpha_{\text{Snow, and, Ice}}$ values, observed during the warm seasons, against $\alpha_{\text{Bare,Ice}}$, obtained using the model parameterizations for summer data as a function of ice thickness. Here, data points tend to lie below the 1:1 line, showing that assuming bare ice alone underestimates surface albedo in the presence of residual snow. This underestimation is especially clear for young ice (diamonds) with moderate snow fractions. Data are in good agreement when the observed snow cover is consistent with the bare ice definition (dark blue dots). Together, panels (a) and (b) demonstrate that both the dry snow and bare ice assumptions introduce systematic biases when applied uniformly for a specific season, and they fail to account for the heterogeneity of surface conditions observed in the MIZ. Panels (c) and (d) further examine the dependence of corrected albedo ($\tilde{\alpha}_{\text{SnowandIce}}$) on ice thickness (h_i), for winter (panel c) and spring/summer (panel d), respectively. These albedo values are corrected for sea ice concentration and solar zenith angle to enable more direct comparison across conditions. In panel (c), most data points approach the dry snow reference orange line ($\alpha = 0.79$ from Lindsay [2001]) at higher thicknesses, but values vary widely at lower thicknesses ($h_i < 0.5\text{m}$), particularly in scenes with low snow cover (darker blue). This indicates that thin ice surfaces are highly sensitive to fractional snow cover, with albedo values ranging from ~ 0.2 to 0.7 depending on snow presence. In panel (d), the theoretical logarithmic relationship (in orange) between bare

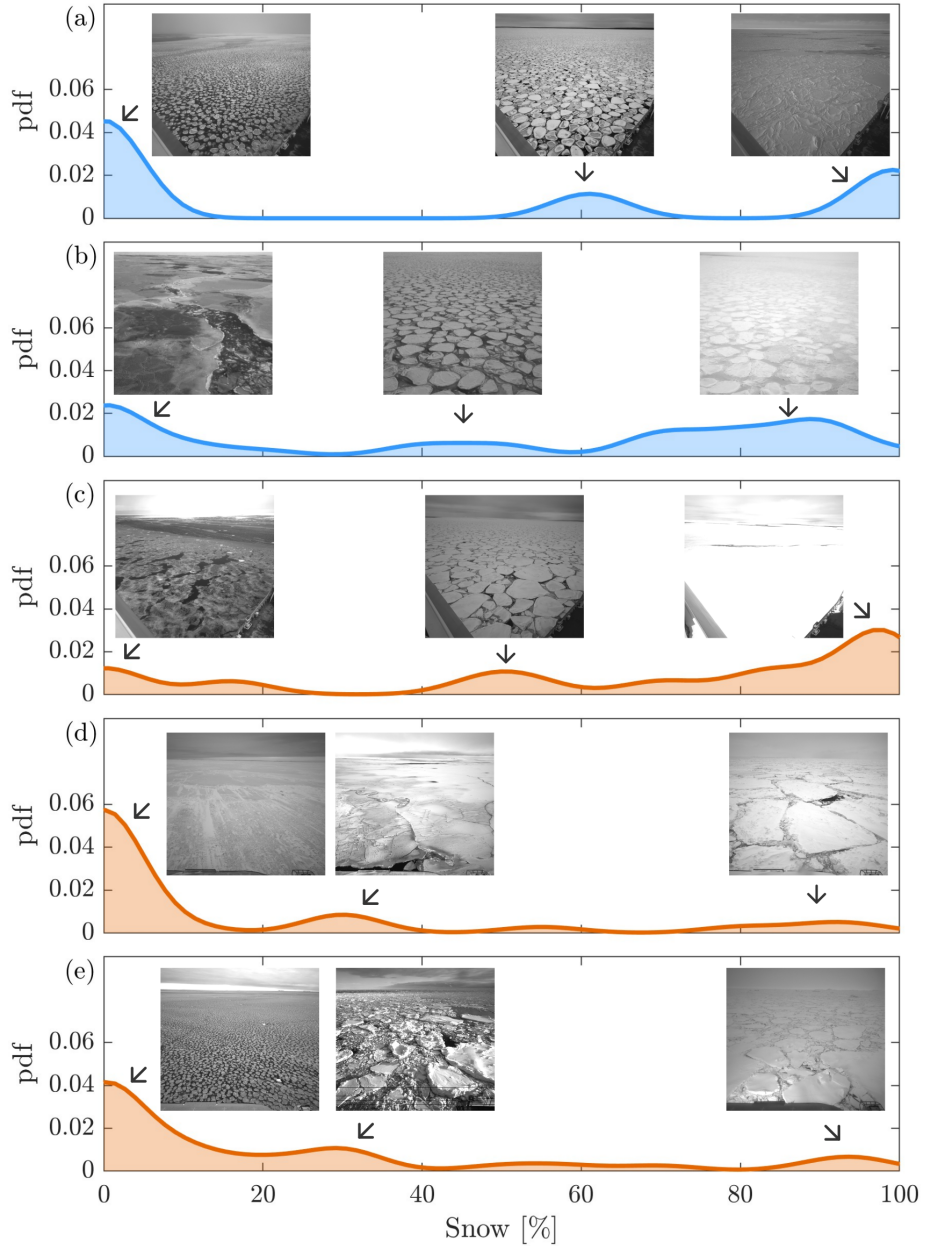


Figure 3: Seasonal distributions of fractional snow cover derived from visible imagery for five Antarctic expeditions. Panels (a–e) show probability density functions (pdf) of snow fraction for July 2019, July 2022, October–November 2019, October–November 2024, and February–March 2024, respectively. Above each plot, representative greyscale visible images illustrate the typical sea ice conditions observed.

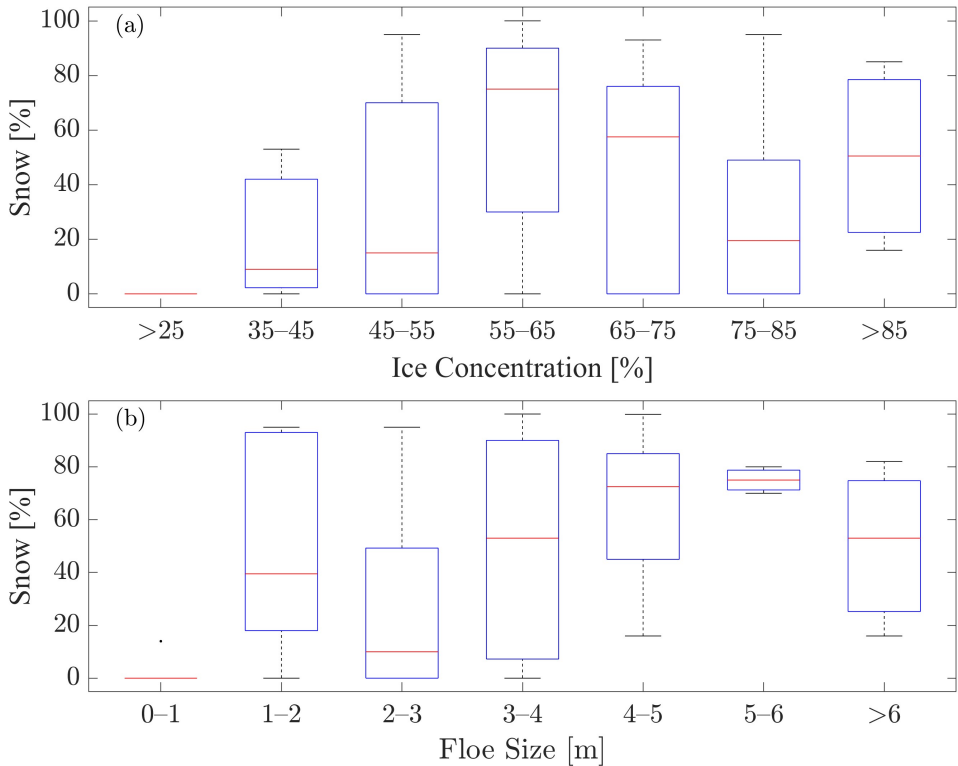


Figure 4: Boxplots of snow cover (%) as a function of (a) sea ice concentration and (b) floe size. In panel (a), ice concentration is binned into seven classes: >25%, 35–45%, 45–55%, 55–65%, 65–75%, 75–85%, and >85%. In panel (b), floe size is binned into seven classes: 0–1 m, 1–2 m, 2–3 m, 3–4 m, 4–5 m, 5–6 m, and >6 m. Boxes represent the interquartile range (25th–75th percentiles), red lines indicate the median, and whiskers show the full data range excluding outliers.

ice albedo and ice thickness under full ice conditions Grenfell [1983] is shown. Observed albedo values exceed this bare ice curve when the snow cover percentage is >0 . The presence of snow, even in small amounts, substantially increases surface reflectivity. Notably, the variability of the albedo is large even at fixed thickness, underscoring the importance of including snow fraction explicitly in albedo parameterizations rather than relying solely on ice thickness. Overall, the results in Figure 5 demonstrate that existing binary or single-variable parameterizations fail to capture the observed complexity of sea ice surface albedo. Our findings highlight the dominant role of snow cover, even in small fractions, in modulating surface reflectivity and emphasize the need for multi-component schemes that incorporate surface type composition and fractional coverage. This is particularly crucial in the MIZ, where thin ice and mixed surfaces are prevalent and small changes in snow cover can result in large changes in radiative forcing.

4 Discussion and Conclusions

Our analysis reveals that snow cover over Antarctic sea ice is highly variable in both space and time, defying the conventional seasonal classifications of dry snow in winter and bare ice in summer. Observations from five field campaigns consistently show the prevalence of fractional snow cover, particularly in the marginal ice zone (MIZ), where episodic snowfall, strong winds, and dynamic ice formation foster a patchy distribution. Snow tends to accumulate on thicker and more stable floes, while thinner ice types such as nilas and pancakes often remain exposed, resulting in persistent heterogeneity even within the same seasonal window. This structured surface variability highlights a fundamental shortcoming of the binary schemes used in many climate models, which assign fixed surface properties such as albedo or thermal conductivity based solely on season or ice thickness. These simplifications fail to capture the complexity of real-world surface conditions, particularly in regions where snow and bare ice frequently coexist. Our findings show that even small fractions of snow can meaningfully alter the radiative and conductive behavior of the sea ice surface. This leads to nonlinear changes in the surface energy budget and introduces systematic biases when snow cover heterogeneity is not resolved. To quantify these impacts, Figures 6 and 7 compare surface energy fluxes calculated under realistic mixed snow–ice conditions (x-axes) with fluxes computed under model assumptions: bare ice in summer (Figure 6) and fully snow-covered ice in winter (Figure 7).

As discussed in Figure 5, the snow fraction on sea ice strongly influences surface albedo, which in turn modulates the reflectance of incoming solar radiation. Since albedo directly controls shortwave absorption F_{sw} , its representation plays a key role in estimating the surface energy budget. Figure 6(a) illustrates that assuming a bare ice surface during the warm seasons leads to a systematic overestimation of the absorbed shortwave flux. The mean bias error (MBE) is $-41.10 W m^{-2}$, corresponding to an average overestimation of approximately 16.4%, relative to the observed snow–ice composite surface. The percentage discrepancy increases with snow cover, and individual deviations reach up to -80% in extreme cases, particularly for data points with high snow fraction. Conversely, in winter (Figure 7(a)), assuming a fully snow-covered surface results in an underestimation of the absorbed shortwave flux. Here, the MBE is $12.99 W m^{-2}$, corresponding to an average underestimation of approximately 16.2%. The discrepancy is more pronounced for low-irradiance conditions, with individual data points showing deviations up to +100% when compared to observations that include partial bare ice cover. The conductive heat flux, F_c , is essential in the estimation of sea ice growth and decay and here the snow layer plays a pivotal role due to its thermal conductivity. F_c decreases with increasing snow cover, reflecting the insulating role of snow. Snow-covered surfaces exhibit reduced upward heat transfer from the ocean to the atmosphere. In contrast, thin or snow-free surfaces allow higher conductive losses, contributing to enhanced ice growth under winter conditions. Figure 6(b) shows how assumptions about surface composition affect conductive heat flux through sea ice during the warm season. When the surface is assumed to be bare ice, the conductive flux is systematically

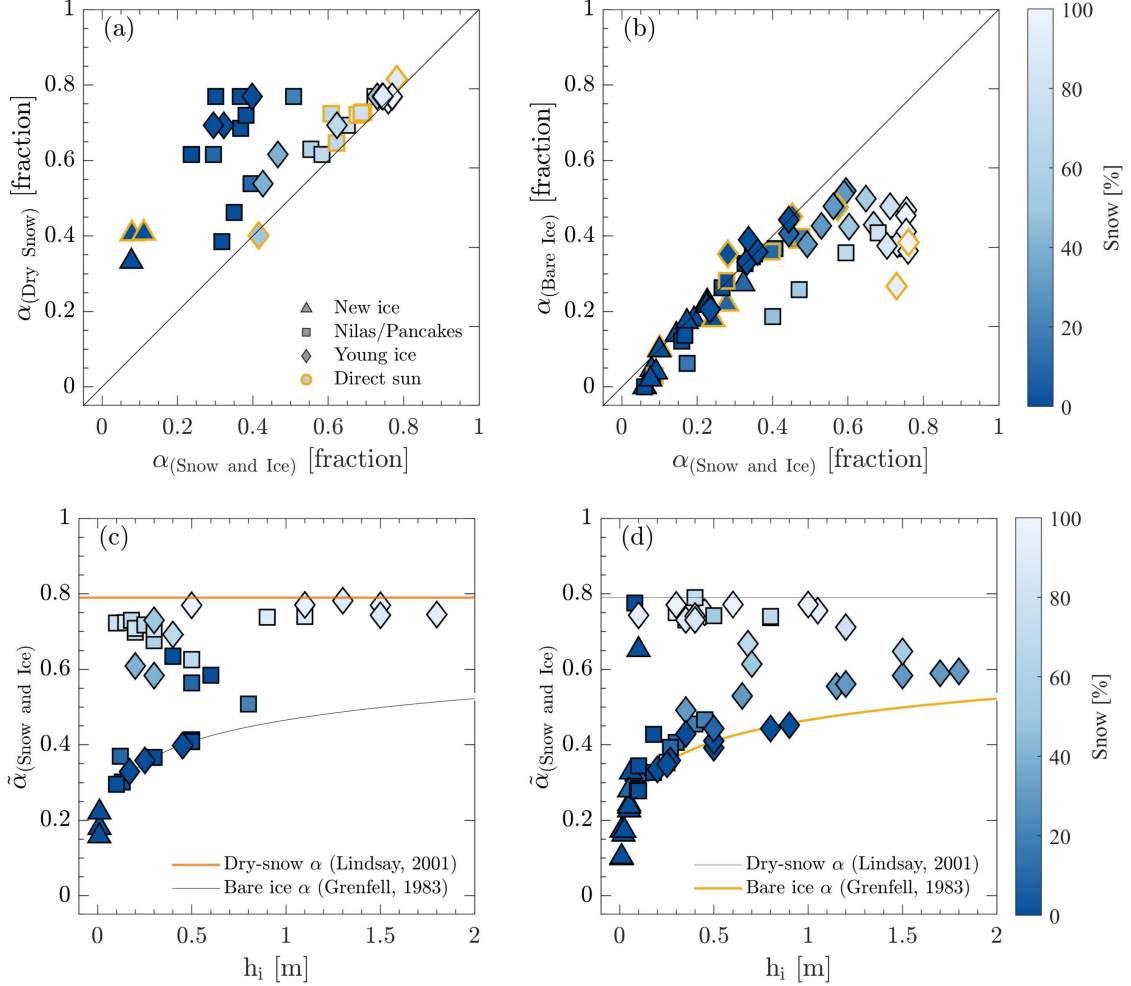


Figure 5: Comparison of surface albedo (α) under different assumptions and conditions.(a) and (b) show the relationship between the surface albedo weighted on the portion of snow and ice($\alpha_{\text{Snow and Ice}}$) x-axes versus the surface albedo assuming a dry snow surface for winter seasons ($\alpha_{\text{Dry Snow}}$) and a bare ice surface for spring/summer seasons ($\alpha_{\text{Bare Ice}}$), respectively.Marker shapes represent surface type categories: new ice (triangles), nilas/pancakes (squares), young ice (diamonds), and markers outlined in yellow indicate direct sun conditions. Dot color indicates snow cover percentage from field observations. The 1:1 line in (a) and (b) indicates perfect agreement. (c) and (d) show the observed surface albedo $\tilde{\alpha}_{\text{(Snow and Ice)}}$ (y-axes) as a function of ice thickness (h_i , x-axes) for winter and spring/summer seasons, respectively. $\tilde{\alpha}$ represents the albedo corrected for the effects of sea ice concentration and solar zenith angle. In winter, the reference line for dry-snow albedo at 0.79 Lindsay [2001] under full ice conditions is shown in orange. In spring and summer, the logarithmic curve illustrates the theoretical relation between bare ice albedo and ice thickness under full ice conditions Grenfell [1983].

overestimated relative to the observed snow–ice surface composition. The mean bias error is -3.92 W m^{-2} , corresponding to an average overestimation of approximately 71%. This discrepancy arises because snow, with its lower thermal conductivity, reduces heat transfer through the surface. Individual data points show a wide spread, with percentage discrepancies ranging from -50% (bare ice underestimation) to +200% (severe overestimation). These results highlight the strong insulating effect of snow and the importance of accounting for its spatial variability when estimating conductive heat fluxes in summer conditions. In winter (7b), dry snow assumption leads to a modest average overestimation of the flux compared to the observed snow–ice surface mix, with a mean bias error of $+1.74 \text{ W m}^{-2}$, equivalent to a 6.7% average discrepancy. The net longwave radiation flux F_l , shown in panels (c) of Figures 6 and 7, exhibits smaller yet systematic discrepancies when simplified surface assumptions are applied. During spring and summer (Figure 6c), the bare ice model leads to a consistent overestimation of emitted longwave energy relative to the observed snow and ice composite. The mean bias error (MBE) is -3.47 W m^{-2} , with a root mean square error (RMSE) of 3.83 W m^{-2} , indicating modest deviations that nonetheless scale with snow fraction. This effect arises because bare ice surfaces, being generally warmer than snow-covered ones, emit more longwave radiation. As snow increases surface reflectivity and reduces solar heating, snow-covered areas maintain lower skin temperatures, thereby reducing longwave emission. A similar trend is observed under winter conditions (Figure 7c), where assuming a fully snow-covered surface leads to a mild underestimation of F_l in cases where partial bare ice exposure increases surface temperature. Although the deviations are smaller than those observed in the shortwave and conductive flux components, they still reflect the sensitivity of longwave emission to skin temperature, which is strongly modulated by surface composition and snow fraction. Overall, the presence of snow lowers the surface temperature and suppresses longwave losses compared to a bare ice assumption. The latent heat flux F_e , shown in panels (d) of Figures 6 and 7, exhibits relatively small magnitudes across all conditions and minimal sensitivity to snow fraction. During the spring and summer season (Figure 6d), the assumption of a bare ice surface introduces a mean bias error (MBE) of -5.84 W m^{-2} and an RMSE of 6.57 W m^{-2} compared to the snow–ice composite. Although this bias is modest in absolute terms, it reflects systematic differences in surface specific humidity and temperature between snow-covered and bare ice areas. Snow tends to suppress moisture exchange due to its lower surface temperature and vapor pressure, leading to weaker sublimation fluxes. Under winter conditions (Figure 7d), discrepancies remain small and mostly confined to scenes with partial snow cover. The dry snow assumption slightly underestimates F_e when bare ice is present, due to its comparatively warmer and more humid surface. Nevertheless, latent heat exchange remains a secondary contributor to the total surface energy budget in both seasons, with the overall flux near zero in most cases. These results confirm that F_e is generally low in cold, snow-covered environments and only marginally affected by variations in snow fraction. The sensible heat flux F_s , presented in panels (e) of Figures 6 and 7, shows moderate variability and a systematic dependence on surface type. During the warm season (Figure 6e), assuming a bare ice surface leads to a consistent overestimation of F_s relative to the snow and ice composite reference. The mean bias error is -6.28 W m^{-2} and the RMSE is 8.06 W m^{-2} . This bias reflects the higher thermal contrast between the atmosphere and the warmer bare ice surface, which enhances upward sensible heat flux. In contrast, snow-covered areas—being cooler—reduce this gradient, thereby lowering the turbulent exchange of sensible heat. In winter (Figure 7e), differences between the dry snow assumption and the observed snow and ice surface composition are less pronounced, but still evident in mixed scenes. Under these conditions, partially exposed bare ice introduces warmer surface patches, slightly increasing F_s relative to a fully snow-covered assumption. Although the absolute magnitude of this bias is smaller than for radiative and conductive components, these cumulative differences can affect boundary layer processes and surface-atmosphere coupling, particularly in regions with fragmented ice and patchy snow distribution. The total surface energy budget F_T , shown in panels (f) of Figures 6 and 7, integrates

the contributions of all radiative and turbulent flux components and thus reflects the cumulative impact of surface representation. In spring and summer conditions (Figure 6f), assuming a bare ice surface leads to a substantial overestimation of the net energy gain by the surface. The mean bias error reaches -60.61 W m^{-2} , with an RMSE of 87.35 W m^{-2} , indicating that simplified surface assumptions significantly distort the energy budget. These discrepancies grow with snow fraction, as even modest snow presence increases albedo and reduces conductive and turbulent fluxes. In winter (Figure 7f), the inverse assumption of a fully snow-covered surface similarly introduces bias, though of smaller magnitude. Scenes with partial bare ice exposure exhibit higher observed net fluxes than those predicted by the dry snow model, due to enhanced shortwave absorption and reduced thermal insulation. These deviations highlight the nonlinear influence of snow cover on surface energy exchange: neglecting its variability can lead to misrepresentation of the energy available for ice melt or growth. Taken together, these results demonstrate that the treatment of snow cover exerts a first-order control on the surface energy budget. Binary assumptions—bare ice or dry snow—fail to capture the flux gradients driven by fractional snow cover, especially in the MIZ where mixed surfaces dominate. Accurate representation of snow heterogeneity is therefore essential for resolving the thermodynamic evolution of Antarctic sea ice.

The findings presented here demonstrate that snow cover heterogeneity exerts a first-order control on the Antarctic sea ice energy budget. Even modest deviations from uniform surface assumptions lead to systematic biases across all flux components, with implications for simulating sea ice growth and decay in climate models. This effect is particularly pronounced in the Marginal Ice Zone (MIZ), where mixed surface types dominate and small variations in snow fraction can drive nonlinear changes in surface albedo and thermal behavior. Our results advocate for a shift away from binary parameterizations toward multi-component surface schemes that resolve fractional snow cover and its influence on energy exchange. Incorporating this complexity into global and regional models will improve the representation of radiative and conductive processes in polar regions and enhance projections of seasonal sea ice evolution under a changing climate. Future efforts should focus on extending observational datasets to include different sectors of the Antarctic and exploring the coupling between snow heterogeneity, atmospheric boundary layer dynamics, and oceanic feedbacks. High-resolution remote sensing and autonomous platforms could help characterize sub-grid variability and inform parameterizations for next-generation Earth system models. Ultimately, reducing these structural uncertainties is critical for accurately assessing polar amplification and its global climate implications.

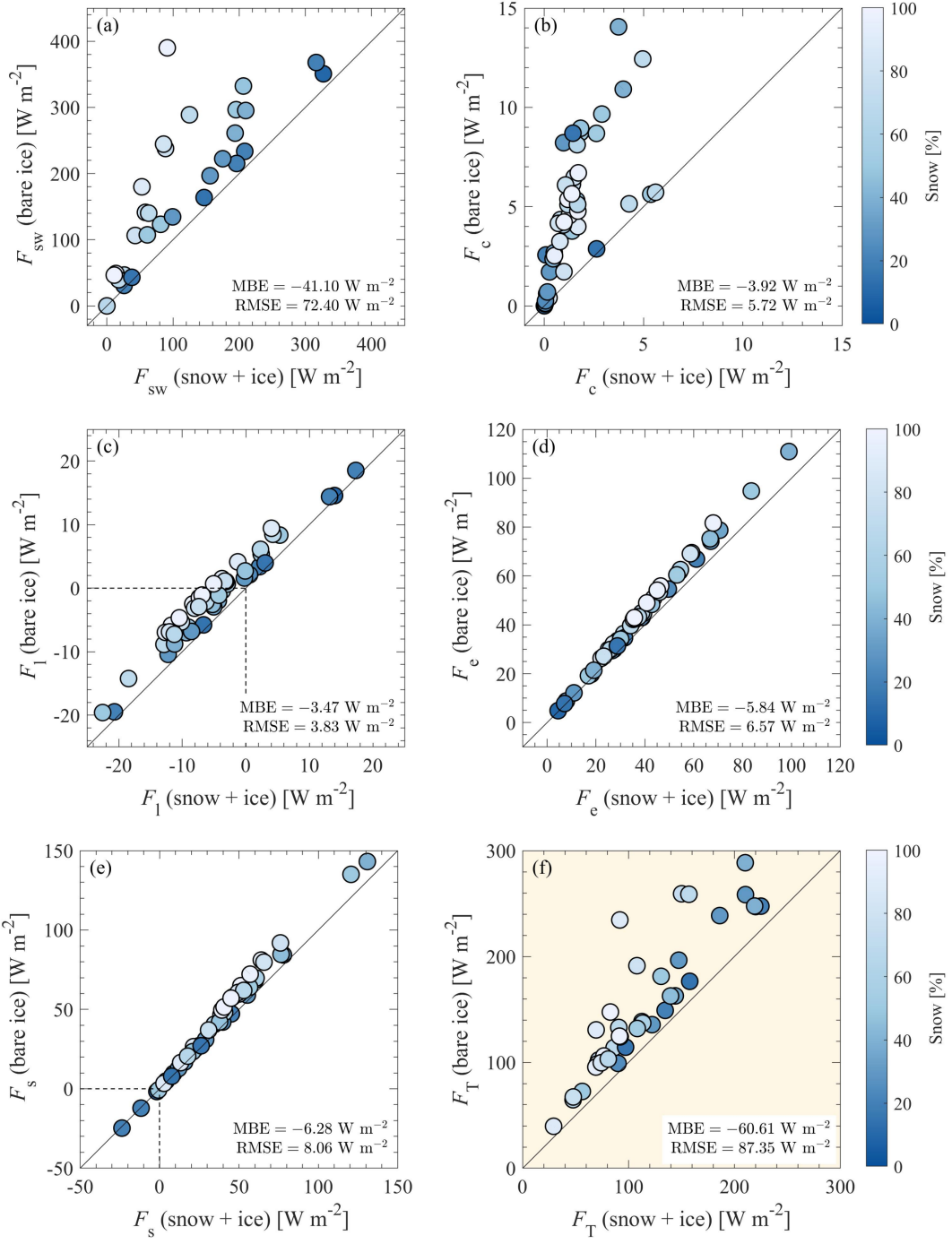


Figure 6: Comparison of surface energy flux components calculated over mixed snow + ice surfaces versus bare ice surfaces during spring and summer conditions. Each subplot presents a scatterplot of fluxes derived using fractional snow cover observations (x-axes) against fluxes assuming an entirely bare ice surface (y-axes). Point color represents the fraction of snow cover, ranging from 0% (dark blue) to 100% (light blue). The black line in each panel represents the 1:1 reference line. **(a)** Shortwave radiative flux F_{sw} ; **(b)** Conductive heat flux F_c ; **(c)** Net Longwave radiation F_l ; **(d)** Latent heat flux F_e ; **(e)** Sensible heat flux F_s ; **(f)** Surface energy budget: $F_T = F_{\text{sw}} + F_l + F_c + F_e + F_s$.

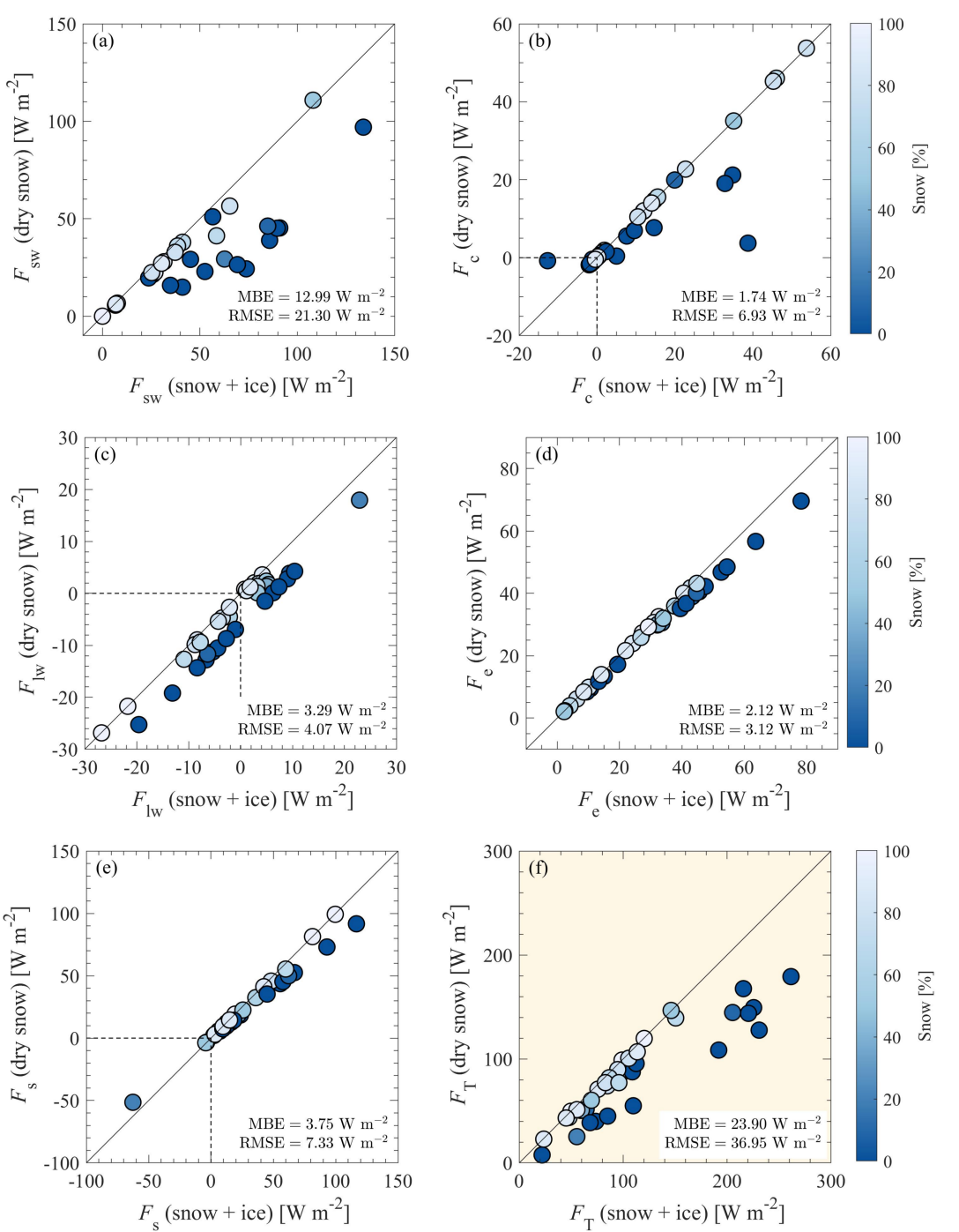


Figure 7: Comparison of surface energy flux components calculated over mixed snow + ice surfaces versus dry snow surfaces during winter conditions. Each subplot presents a scatterplot of fluxes derived using fractional snow cover observations (x-axes) against fluxes assuming an entirely dry snow surface (y-axes). Data symbols, flux notation, and color scale are consistent with the spring/summer panel 6.

References

- Alberto Alberello, Miguel Onorato, Luke Bennetts, Marcello Vichi, Clare Eayrs, Keith MacHutchon, and Alessandro Toffoli. Brief communication: Pancake ice floe size distribution during the winter expansion of the antarctic marginal ice zone. *The Cryosphere*, 13(1):41–48, 2019.
- Alberto Alberello, Luke G Bennetts, Miguel Onorato, Marcello Vichi, Keith MacHutchon, Clare Eayrs, Butteur Ntamba Ntamba, Alvise Benetazzo, Filippo Bergamasco, Filippo Nelli, et al. Three-dimensional imaging of waves and floes in the marginal ice zone during a cyclone. *Nature Communications*, 13(1):4590, 2022.
- I. Allison. Antarctic sea ice thickness monitoring by ships. Workshop on Antarctic Sea Ice Thickness Monitoring, 1989. Hobart, Australia.
- Yevgeny Batrak and Martin Müller. Modeling the arctic snow and sea ice albedo using a coupled atmosphere-sea ice-snow model with a multilayer snow scheme. *Journal of Advances in Modeling Earth Systems*, 10(11):2743–2759, 2018. doi: 10.1029/2018MS001415.
- Richard E. Brandt and Stephen G. Warren. Solar-heating rates and temperature profiles in antarctic snow and ice. *Journal of Glaciology*, 39(131):99–110, 1993.
- Michael A Brunke, Mingyu Zhou, Xubin Zeng, and Edgar L Andreas. An intercomparison of bulk aerodynamic algorithms used over sea ice with data from the surface heat budget for the arctic ocean (sheba) experiment. *Journal of Geophysical Research: Oceans*, 111(C9), 2006.
- Michael A Brunke, Zhuo Wang, Xubin Zeng, Michael Bosilovich, and Chung-Lin Shie. An assessment of the uncertainties in ocean surface turbulent fluxes in 11 reanalysis, satellite-derived, and combined global datasets. *Journal of Climate*, 24(21):5469–5493, 2011.
- Neige Calonne, Lucas Millancourt, Alexis Burr, Armelle Philip, Christophe L Martin, Frederic Flin, and Christian Geindreau. Thermal conductivity of snow, firn, and porous ice from 3-d image-based computations. *Geophysical Research Letters*, 46(22):13079–13089, 2019.
- Emiliano Cimoli, Marco Marcer, Baptiste Vandecrux, Carl E Bøggild, Guy Williams, and Sebastian B Simonsen. Application of low-cost uass and digital photogrammetry for high-resolution snow depth mapping in the arctic. *Remote Sensing*, 9(11):1144, 2017.
- Emiliano Cimoli, Klaus M Meiners, Arko Lucieer, and Vanessa Lucieer. An under-ice hyperspectral and rgb imaging system to capture fine-scale biophysical properties of sea ice. *Remote Sensing*, 11(23):2860, 2019.
- Emiliano Cimoli, Vanessa Lucieer, Klaus M Meiners, Arjun Chennu, Katerina Castrisios, Ken G Ryan, Lars Chresten Lund-Hansen, Andrew Martin, Fraser Kennedy, and Arko Lucieer. Mapping the in situ microspatial distribution of ice algal biomass through hyperspectral imaging of sea-ice cores. *Scientific Reports*, 10(1):21848, 2020.
- Todd M Crawford and Claude E Duchon. An improved parameterization for estimating effective atmospheric emissivity for use in calculating daytime downwelling longwave radiation. *Journal of Applied Meteorology*, 38(4):474–480, 1999.
- Judith A Curry, Jeffrey L Schramm, and Edwin E Ebert. Sea ice-albedo climate feedback mechanism. *Journal of Climate*, 8(2):240–247, 1995.
- Emanuel Dutra, Gianpaolo Balsamo, Pedro Viterbo, Pedro M. A. Miranda, Anton Beljaars, Christoph Schär, and Kelly Elder. An improved snow scheme for the ecmwf land surface

model: Description and offline validation. *Journal of Hydrometeorology*, 11(4):899–916, 2010. doi: 10.1175/2010JHM1249.1.

Elizabeth E Ebert and Judith A Curry. An intermediate one-dimensional thermodynamic sea ice model for investigating ice-atmosphere interactions. *Journal of Geophysical Research: Oceans*, 98(C6):10085–10109, 1993.

ECMWF. IFS Documentation CY47R3: Part IV: Physical processes. Technical report, European Centre for Medium-Range Weather Forecasts, 2021. URL https://www.ecmwf.int/sites/default/files/elibrary/2021/81271-ifs-documentation-cy47r3-part-iv-physical-processes_1.pdf.

Darren Eustace, Stephen English, Richard Forbes, et al. Evaluating biases in sea ice albedo climatologies in reanalysis and forecasting systems: implications for surface energy budget simulations. *Atmospheric Chemistry and Physics*, 24:4157–4175, 2024. doi: 10.5194/acp-24-4157-2024.

Thomas C Grenfell. A theoretical model of the optical properties of sea ice in the visible and near infrared. *Journal of Geophysical Research: Oceans*, 88(C14):9723–9735, 1983.

C Horvat and E Tziperman. A model for the seasonal evolution of the sea ice floe size distribution. *The Cryosphere*, 9(6):2119–2134, 2016.

Muhammad Iqbal. *An introduction to solar radiation*. Elsevier, 2012.

John TO Kirk. *Light and photosynthesis in aquatic ecosystems*. Cambridge university press, 1994.

Bonnie Light, Gary A Maykut, and Thomas C Grenfell. The optical properties of arctic and antarctic sea ice. *Journal of Geophysical Research: Oceans*, 103:1153–1170, 2008.

RW Lindsay. Arctic sea-ice albedo derived from rgps-based ice-thickness estimates. *Annals of Glaciology*, 33:225–229, 2001.

Robert A Massom and Sharon E Stammerjohn. Snow on antarctic sea ice. *Reviews of Geophysics*, 38(3):407–430, 2001.

Gary A. Maykut and Norbert Untersteiner. Some results from a time-dependent thermodynamic model of sea ice. *Journal of Geophysical Research*, 76(6):1550–1575, 1971. doi: 10.1029/JC076i006p01550.

Francis W Murray. On the computation of saturation vapor pressure. *Journal of Applied Meteorology and Climatology*, 6(1):203–204, 1967.

Marcel Nicolaus, Christian Katlein, James Maslanik, and Stefan Hendricks. Seasonal changes of spectral albedo and transmittance of arctic sea ice in the central arctic ocean. *The Cryosphere*, 4(4):431–446, 2010.

Dirk Notz and Julienne Stroeve. Observations reveal external driver for arctic sea-ice retreat. *Geophysical Research Letters*, 43(20):10,280–10,288, 2016.

Giulio Passerotti, Alberto Alberello, Marcello Vichi, Luke G Bennetts, James Bailey, and Alessandro Toffoli. Segmenting sea ice floes in close-range optical imagery with active contour and foundation models. *arXiv preprint arXiv:2409.06641*, 2024.

T Ryan-Keogh and M Vichi. Scale-win19 & scale-spr19 cruise report. *Southern Ocean Seasonal Cycle Experiment, South Africa*, 2022.

- KP Shine and A Henderson-Sellers. The sensitivity of a thermodynamic sea ice model to changes in surface albedo parameterization. *Journal of Geophysical Research: Atmospheres*, 90(D1): 2243–2250, 1985.
- Vernon A Squire. Ocean wave interactions with sea ice: A reappraisal. *Annual Review of Fluid Mechanics*, 39:195–210, 2007.
- Julienne C Stroeve, Mark C Serreze, Marika M Holland, Jennifer E Kay, Jan Malanik, and Andrew P Barrett. The arctic's rapidly shrinking sea ice cover: a research synthesis. *Climatic Change*, 110:1005–1027, 2012.
- Matthew Sturm, Jan Holmgren, Martin König, and Keith Morris. The thermal conductivity of seasonal snow. *Journal of Glaciology*, 43(143):26–41, 1995.
- Matthew Sturm, Jon Holmgren, Max König, and Kim Morris. The thermal conductivity of seasonal snow. *Journal of Glaciology*, 43(143):26–41, 1997.
- Matthew Sturm, Jan Holmgren, Joe P. McFadden, Glen E. Liston, F. Stuart Chapin, and Charles H. Racine. Winter biological processes in arctic soils: Reflections from a snow perspective. *Biogeochemistry*, 55(1):191–222, 2002. doi: 10.1023/A:1020512225517.
- Lynne D Talley. *Descriptive physical oceanography: an introduction*. Academic press, 2011.
- Ippolita Tersigni, Alberto Alberello, Gabriele Messori, Marcello Vichi, Miguel Onorato, and Alessandro Toffoli. High-resolution thermal imaging in the antarctic marginal ice zone: Skin temperature heterogeneity and effects on heat fluxes. *Earth and Space Science*, 10(9): e2023EA003078, 2023.
- Stephen G Warren, Ignatius G Rigor, Norbert Untersteiner, Vladimir F Radionov, Nikolai N Bryazgin, Yevgeny I Aleksandrov, and Roger Colony. Snow depth on arctic sea ice. *Journal of Climate*, 12(6):1814–1829, 1999.
- Timothy D Williams, Vernon A Squire, Luke G Bennetts, Dany Dumont, and Michael H Meylan. Wave–ice interactions in the marginal ice zone. part 1: Theoretical foundations. *Ocean Modelling*, 71:81–91, 2013.
- Warren J. Wiscombe and Stephen G. Warren. A comparison of the optical properties of snow and cloud. *Journal of the Atmospheric Sciences*, 37(12):2712–2733, 1980. doi: 10.1175/1520-0469(1980)037<2712:ACOTOP>2.0.CO;2.
- Anthony P Worby and Josefino C Comiso. Studies of the antarctic sea ice edge and ice extent from satellite and ship observations. *Remote sensing of environment*, 92(1):98–111, 2004.
- Anthony P. Worby, Cathleen A. Geiger, Michael J. Paget, Michael L. Van Woert, Stephen F. Ackley, and Tracey L. DeLiberty. Thickness distribution of antarctic sea ice. *Journal of Geophysical Research: Oceans*, 113(C5), 2008. doi: 10.1029/2007JC004254.
- AP Worby and Ian Allison. Ocean-atmosphere energy exchange over thin, variable concentration antarctic pack ice. *Annals of Glaciology*, 15:184–190, 1991.